

Effect of Air Swirler Configuration on Lean Direct Injector Flow Structure and Combustion Performance with a 7-point Lean Direct Injector Array

Yolanda R. Hicks, Kathleen M. Tacina, and Robert C. Anderson

Yolanda.R.Hicks@nasa.gov

NASA Glenn Research Center

Engine Combustion Branch

Cleveland Ohio

United States of America

ABSTRACT

Studies of various injector configurations in a 7-point Lean Direct Injector (LDI) array are reported for both non-reacting (cold) flow and for Jet-A/air reacting flows. For cold flow, central recirculation zone (CRZ) formation is investigated and for reacting flows, combustor operability and dynamics are of interest. 2D Particle Image Velocimetry (PIV) measurements are described for the cold flow experiments and flame chemiluminescence imaging and dynamic pressure results are discussed for the reacting flow cases. PIV results indicate that for this configuration the close spacing between swirler elements leads to strong interaction that affects whether a CRZ forms, and pilot recess and counter-swirl helps to isolate swirlers from one another. Dynamics results focus on features identified near 500-Hz.

Keywords: gas turbine combustors; fuel injection; fluid mixing

NOMENCLATURE

| | |
|------------------|--------------------------------|
| c | Center (swirler) |
| C ₂ * | Diatomic carbon radical |
| CH* | CH radical |
| CCW | Counterclockwise (swirl) |
| CRZ | Central Recirculation Zone |
| CW | Clockwise (swirl) |
| LDI | Lean Direct Injection/Injector |
| LH | Left-Hand (swirl, swirlers) |
| f | Focal length |
| f/ | f-number, f-stop |
| NO _x | Oxides of Nitrogen |
| o | Outer (swirlers(s)) |
| P, p | pressure |
| PIV | Particle Image Velocimetry |
| RH | Right-Hand (swirl, swirlers) |
| SN | Swirl Number |
| T | temperature |
| U _{ref} | Cold flow reference velocity |
| V | velocity |
| 3 | Combustor inlet |
| 4 | Combustor exit |

Symbols

| | |
|--------|--------------------------------------|
| ϕ | Equivalence ratio, fuel-to-air basis |
| x | Horizontal coordinate x |
| y | Horizontal coordinate y |
| z | Vertical coordinate z |

1.0 INTRODUCTION

Lean Direct Injection (LDI) describes a fuel-air mixing and combustion concept to keep aircraft combustor emissions of oxides of nitrogen (NO_x) as low as possible. In LDI, fuel is injected directly into the air at the front-end of the combustor without subsequent addition of air downstream. Thus, the combustor does not have a rich front end and is fuel-lean throughout. Several small injector elements replace a single, more traditional fuel air mixer, enabling more evenly distributed fuel and shorter flames. NASA began a concerted study of LDI during the High Speed Research (HSR) Program in the 1990s, which demonstrated its viability as a technique. During this time, the first generation, LDI-1 was designed. The overall cross section was 76.2-mm x 76.2-mm (3-in by 3-in). LDI-1 can be characterized as having all elements the same size, with a simple grid arrangement of elements (3 x 3), (4 x 4), etc., and having all fuel nozzles of the same type. There was no distinct pilot where one injector is installed slightly upstream of the other elements. The convenient size of the 3 x 3 array fit into available flame tube facilities where combustion studies were done and various ways of mixing the fuel and air have been examined [1-3]. The baseline LDI-1 is a 3 x 3, 9-pt LDI that uses axial air swirlers and simplex fuel nozzles, and is described in [4].

LDI-2 extended the LDI-1 operability range through use of a pilot fuel/air mixer, and replacing some simplex nozzles with airblast nozzles, as described by Ajmani et al. [5], and Tacina [6-7]. LDI-2 was successfully demonstrated under the Environmentally Responsible Aviation (ERA) Program [7]. Like LDI-1, LDI-2 is contained in a module with square cross section; however the injector elements are arranged in a circle.

The third generation, LDI-3 [8], adds on from the knowledge gained in LDI-2, and incorporates a more practical fuel-stem arrangement for introducing the fuel. The module was developed cooperatively with Woodward, FST and tested at NASA. The module is a 3-cup sector which was designed for small core engines.

Although the use of LDI in the HSR and ERA programs was successful in terms of reaching the NO_x emissions goals, there is still room for reduction, particularly as regulations become more stringent. NASA N+3 goals for

small core engines provide technical challenges due to the tighter packing required for the smaller cores. Thus, the objectives of the 7-pt LDI experiments—to develop a better understanding of how the LDI elements interact, and to determine their effect on flow structure and pursuant combustion and dynamics—mesh well with the objectives of focused programs such as the Advanced Air Transportation Project (AATT).

A drawback of fuel-lean combustion is susceptibility to instabilities and combustion dynamics [9, 10]. Some unsteadiness may be caused by swirling flow, which is typically used in gas turbine combustors in order to establish a central recirculation zones (CRZ). CRZs are used to promote fuel-air mixing and help hold the flame in place. The CRZ is associated with a precessing vortex core, in which the axis of rotation of the swirling flow is itself rotation around the geometric center of the flow field [11, 12].

In earlier studies using a single point LDI [13] (see figure 1), we determined that the 60° swirler produced a CRZ, while the 45° and 52° swirlers did not. Recirculation zone formation was consistent with our testing of a corresponding 9-point array, the baseline LDI-1 configuration, in which we saw a CRZ behind all 60° swirlers [14, 15] (we never tested any other swirler angles with the 9-point). However, when running the 7-point array with all 60° swirlers, we did not see a CRZ behind the center swirler. The three LDI configurations use identical swirlers and the fuel nozzles have the same size envelope, but the chamber shape and swirler spacing is different.

The lack of a CRZ behind the 7-point center swirler led us to posit two possible, but not mutually-exclusive reasons. One possibility is that the spacing between elements is close enough that interactions between the swirlers prevents a center swirler CRZ from forming. Another possibility is that the circular combustion chamber has an effect. The facility construction is such that we cannot easily shift to a square or rectangular cross section, so we cannot really test for a chamber shape effect. In the first phase of our parametric survey using the 7-point LDI to assess (in part) the proximity effect [16], we used screens in place of some swirler, as a way to change spacing. In some configurations, we offset the center swirler. Because the single-point LDI test showed the field downstream of the 45° swirler had little radial spread, we tried 45° swirlers all around, or alternating with 60° swirlers. In our second round of parametric testing, we added the 52° swirlers to the parameter set, and were able to conduct limited burning tests. There remain a few more configurations to test under cold flow conditions, followed by completing the burning tests of selected configurations.

The 7-pt LDI used in the current work is of type LDI-1 in that all elements are the same size. Since we consider the 9-pt LDI as our baseline for comparison, we use the same swirlers as used in the 9-pt, and the simplex fuel nozzles have the same outer dimensions. The 7-pt LDI is different than the 9-pt LDI in that the elements have a circular arrangement, as with LDI-2 and LDI-3. The center element of the 7-pt LDI may also be offset, to act as a pilot, of sorts. One feature different from all the others is that the center-to-center distance between all adjacent elements is the same for the 7-point, and this distance is smaller compared to all the others. One other difference is that the current 7-pt LDI arrangement is tested in a circular tube; all other configurations have been tested in rectilinear flame tubes.

This paper describes work that includes a parametric study looking at the effect of air swirler angle, position, center offset and orientation (left-handed versus right-handed). Results from the cold-flow cases focus on the axial velocity flow field. Results for combustng cases focus on combustion dynamics.

2.0 HARDWARE AND EXPERIMENT

2.1 LDI Hardware

The left of figure 1 shows an end view of the 7-pt LDI hardware. Because we make reference to the LDI-1 baseline 9-pt array and to the 1-pt LDI in the discussion, we include those also. All three configurations use an element as described in the schematic drawing on the right. Each element (nominally 25-mm) consists of an axial swirler, converging-diverging venturi and simplex atomizer. The simplex atomizer fits within the hub of the air swirler and its tip is positioned so that the fuel is injected at the venturi throat. The simplex nozzle produces a hollow cone spray with an angle nominally of 70°, and has a flow number, FN_{US} of 0.7. The air swirler has six-helical blades, with a hub diameter of 0.34-in outer diameter of approximately 0.875-inch. The three swirler angle are 60° (baseline), 52°, and 45°. The calculated swirl numbers, as defined by Beer and Chigier [17] are 1.02, 0.77, and 0.59. The venturi throat diameter is 0.5-in. The 7-pt and 1-pt have a venturi throat length of 0.061-in.

The elements of the 7-pt LDI are arranged with a center element surrounded by six equally-spaced elements on the outside in a hexagonal arrangement. The center-to-center spacing between adjacent nozzles (including the center element) is identical.

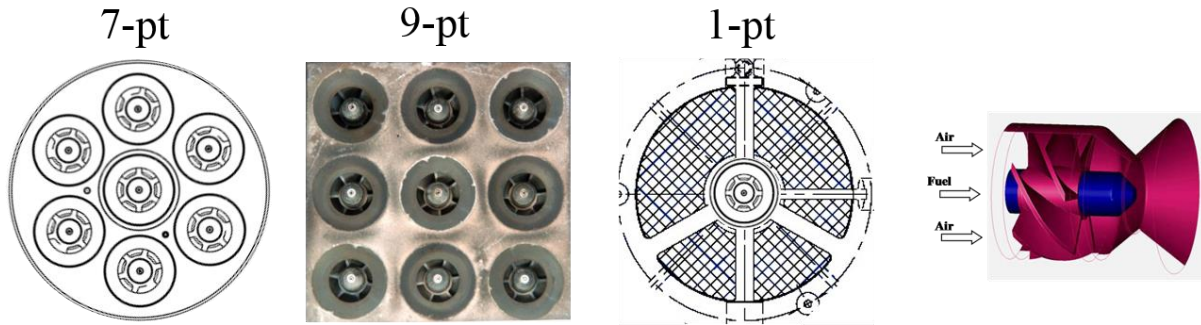


Figure 1 End views of the 7-pt LDI, the baseline 9-pt, and 1-point element arrangements. On right is an isometric drawing that shows the basic components of a single LDI element.

2.2 Test Facility

The facility used was the Combustion and Dynamics Facility (CDF), in which the flow through the combustor passes from top to bottom. The CDF can supply non-vitiated air preheated up to 810 K at air flow rates up to 0.35 kg/sec and pressures up to 517-kPa. Figure 2 (left) shows a plan view of the combustor section. The combustor test section is 15-cm long and has a circular cross-section nominally 7.62-cm in diameter (including the ceramic flame spray coating on the inner circumference). Three sets of double-paned windows, spaced 90° apart around its circumference, provide optical access to the water-cooled combustor. The windows are flat and have a small offset away from the combustor circumference. The windows measure 6.1-cm tall (axial direction) by 5.8-cm wide (azimuthal). On the fourth “side”, the combustor has ports configured for transducers to allow for dynamic pressure measurements. There are five possible positions in all, each at a different axial location, with two on one side and three on the other. Before the combustion products are exhausted, they are cooled using water spray. The first spray nozzle is approximately 520-mm downstream of the combustor dome.

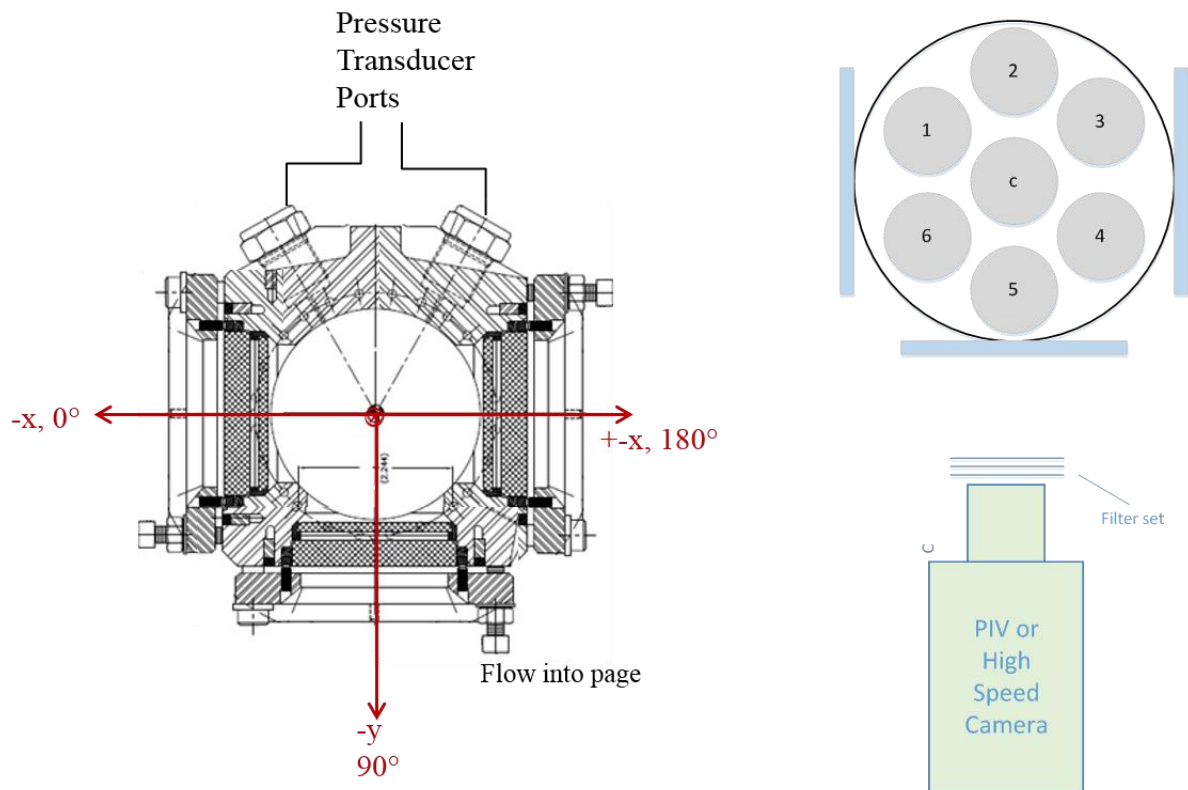


Figure 2 Left: Cross-sectional detail of the combustor that shows the window orientation, defines the coordinate system and shows the locations of the pressure transducer ports. Right: Sketch showing a top view of the imaging system layout and swirler designation and arrangement with respect to the camera.

2.3 Instrumentation and Procedure

Dynamic pressure fluctuations were measured using a cooled, PCB sensor flush-mounted on the combustor wall. Data were recorded using a Data Translation DT9841-sb high-speed data acquisition system, typically at a 60 kHz data acquisition rate for between 30 and 120 seconds. Steady-state data were recorded using Labview.

The optical measurements described here are of 2D velocity using standard PIV during cold flow testing, and of time-resolved flame chemiluminescence during combustion tests. For both measurements, we used an imaging layout similar to that illustrated on the right in figure 2.

When performing PIV, a laser beam was formed into a light sheet using a set of cylindrical lenses. The sheet passed through the test section and aligned parallel with the flow direction. The camera was positioned normal to the laser sheet and collected the light scattered by water droplets. We found it useful to include a neutral density filter in addition to (or in lieu of) a 532-nm interference filter, to help reduce overall brightness from the scattered light. The neutral density filter was especially helpful in blocking the additional light that arrives because of the long second exposure of the camera. The PIV data were acquired using a 15-Hz dual-head, frequency-doubled, Nd:YAG laser and a single, interline transfer, CCD camera. We traversed across the flow in 1-mm increments (generally from $y = -24$ to $y = +24$), and collected 500 image pairs per position. DaVis version 8.3 and PTU versions 9 and 10 (LaVision, Inc.) were used to collect the PIV images. Data were collected were 5-bar, and 700K. Common cold flow reference velocities used for all cold flow tests were 22.9-m/s and 15.2 m/s.

DaVis version 8.1.2 software was used to process the PIV data. The same multi-pass cross-correlation vector processing was used on all data sets. Generally, the windows stayed fairly clean, and using a neutral density filter helped with having both exposures have similar brightness. Although it is not usually necessary for data processing, it helps when taking the data to assess whether both images of the pair are of reasonable quality. For the rare occasions when the window surfaces became dirty or foggy and caused reflections, images were pre-processed by subtracting a sliding background. The processed results are axial horizontal-axial (x-z) components of velocity at each y-position.

For the flame chemiluminescence measurements, we used a 12-bit, high speed CMOS camera ($1k \times 1k$) focused on the vertical center plane. The light collected was largely a combination of CH^* and C_2^* emissions, emitted from the volume and within the field-of-view of the collection optics. We framed at 40,000 per second (exposure time 25- μ s or shorter), with resolution of 320×368 pixels, using an $f = 50$ -mm, $f/1.2$ lens. To block excess light and prevent saturation, we used faster shutter speeds and neutral density filters.

2.4 Swirler configurations tested

We report on nine different configuration variations of the 7-pt array, listed in table 1.

Table 1
Descriptive designations of the 7-pt swirler configuration variations described

| Designation | Center Swirler | Outer Swirlers |
|------------------------|----------------|-----------------------|
| LH60all | LH 60° | LH 60° |
| LH60all_offset | Offset LH 60° | LH 60° |
| RH60c-1-3-5_LH60-2-4-6 | RH 60° | Alternating RH60/LH60 |
| RH60c-1-3-5_RH45-2-4-6 | RH 60° | Alternating RH60/RH45 |
| RH60coff_RH45o | Offset RH 60° | RH 45° |
| RH60c_RH45o | RH 60° | RH 45° |
| LH60c_RH45o | LH 60° | RH 45° |
| RH60c_RH52o | RH 60° | RH 52° |
| RH52all | RH 52° | RH 52° |

3.0 RESULTS AND DISCUSSION

We first describe the cold flow test results, beginning with a description of a typical processed average velocity field, then provide an overview of all configurations at a fixed axial location, followed by selected detailed descriptions. We follow the cold flow discussion with the combustor cases, which includes how stable it seemed to operate, then present combustion dynamics analyses for selected configurations and inlet conditions.

3.1 Typical processed result within a traversed set

Figure 3 shows an example of results obtained at a fixed point within a traverse across the flow. The spatial location is the $y=0$ position, for configuration RH60c_RH45o. Flow passes from top to bottom. The top row shows the resultant vector fields coloured by axial velocity contours for reference velocities 22.9-m/s (left) and 15.2-m/s. The bottom row shows the vector field along with squares representing the axial velocity component: black for the velocity and red for the RMS. All charts have a dash-dot line that indicates the centerline. Although for this phase of our study, we are not looking at the turbulence levels, we see that RMS is high—on the order of the measured velocity—in the recirculation regions, and low where the flow is more uniform. This typical result also reassures us that seeding by use of water injection through the center nozzle is adequate for our objectives.

All images, including those noted above, were post-processed using Tecplot. Typically, the time-averaged velocity fields at each y -position was imported as a data block from DaVis. Generally, we slice the data block in planes orthogonal to the flow and observe the axial velocity field at fixed distances, z , from the dome. Most of the remaining figures will be presented in this fashion. We also present results to more clearly show iso-velocity contours that show the regions of reverse flow.

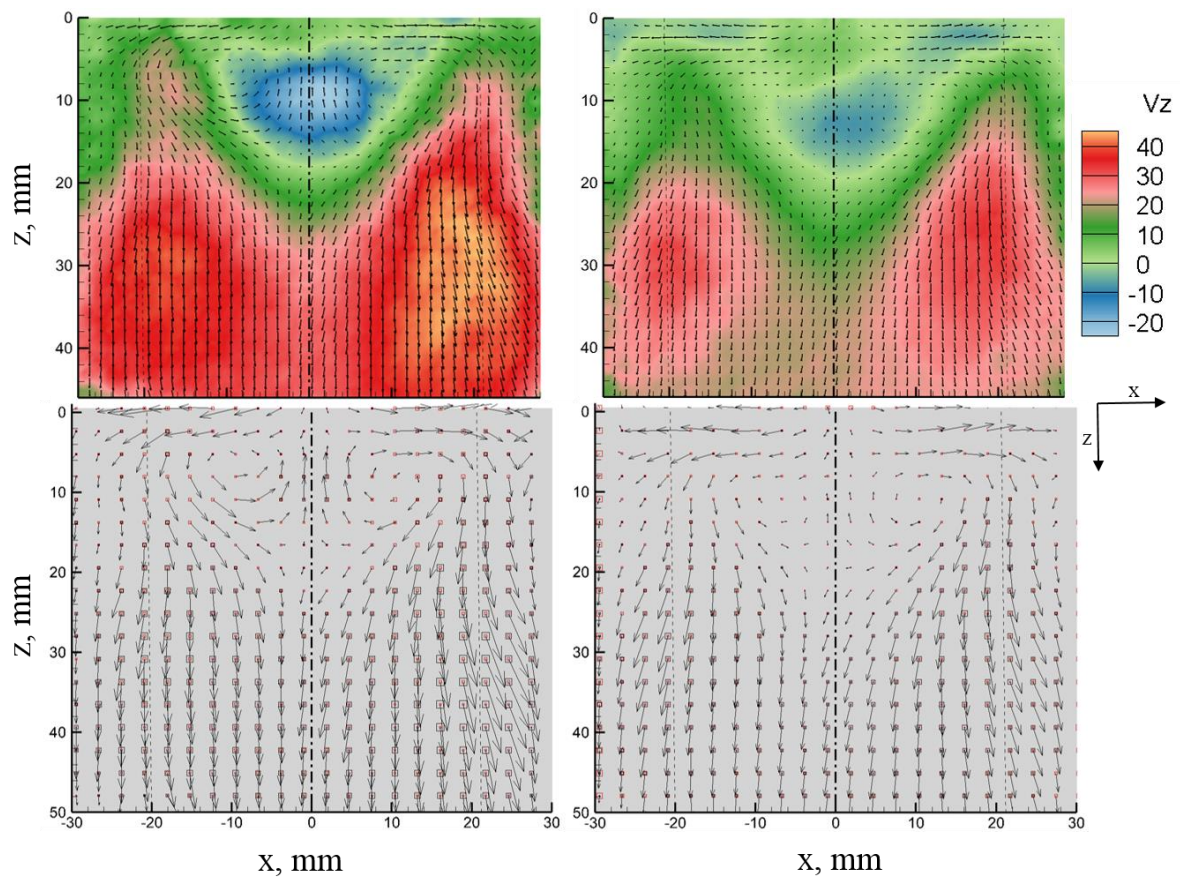


Figure 3 Average horizontal-axial (x, z) velocity fields obtained at $y = 0$ for 7-LDI configuration RH60c_RH45o for two reference velocities (columns). The top row shows the 2-D vector field and axial velocity contour. The bottom row shows the velocity vectors along with squares that are sized according to the axial velocity component (black) or RMS (red). Inlet temperature and pressure are 800K, 5-bar. U_{ref} : 22.9-m/s (left); 15.2-m/s (right)

3.2 Overview of the general features observed for the nine 7-pt LDI swirler configurations

We provide a general description of the cold flow parametric results to date, considering recirculation zone formation. Selected greater detail can be found later in the discussion.

Figures 4 – 6 are summary plots to help describe the average flow structure as represented by the axial velocity field.

Figure 4 shows an overview summary comparison of axial velocity contours approximately 10-mm downstream of the injector dump plane, within the optically-accessible region, for the nine configurations described in this paper. Overlaying the plots are color-coded circles that indicate the positions of the swirlers within the array.

Solid black, purple, and pink represent 60°, 52°, and 45° RH swirlers. Dashed circles represent LH swirlers, and white circles represent the center swirler offset. Although each is individually-scaled, blue always represents reverse flow. The configurations are also identified in the figure caption.

The isometric views shown in figures 5 and 6 are iso-surface contours of $V_z = 0$ for those configurations without and with a center swirler CRZ. The spatial orientations are varied to best show the recirculation regions. For the cases that have outer swirler CRZs, those are cut off because of the limited field-of-view. The surfaces are colored by the axial distance, with blue closest to the dump plane and red farthest away, to provide some context for length. The iso-surfaces have been smoothed to look nice.

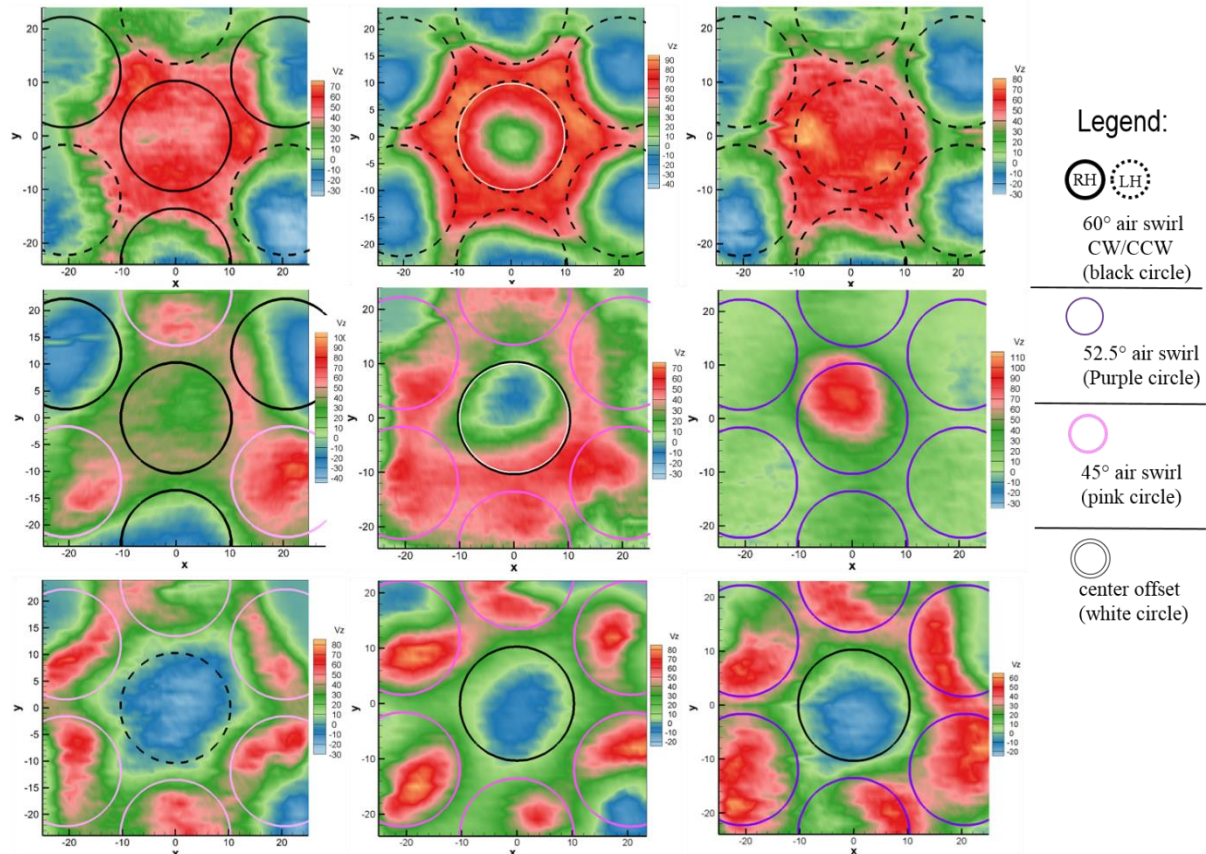


Figure 4 End view composites showing 7-point LDI axial velocity contours approximately 10-mm from the dump plane for nine swirler configurations. The color-coded circles (see legend) indicate the projected locations of each array element. The air inlet conditions were 5-bar, 800K, reference velocity = 22.9 m/s.

Top row: RH60c-1-3-5_LH60-2-4-6; LH60all_coffset;
Center row: RH60c-1-3-5_RH45-2-4-6; RH60coff_RH45o;
Bottom row: LJ60c_RH45o; RH60c_RH45o;

From left to right, the configurations are:

LH60all;
RH52all;
RH60c_RH52o

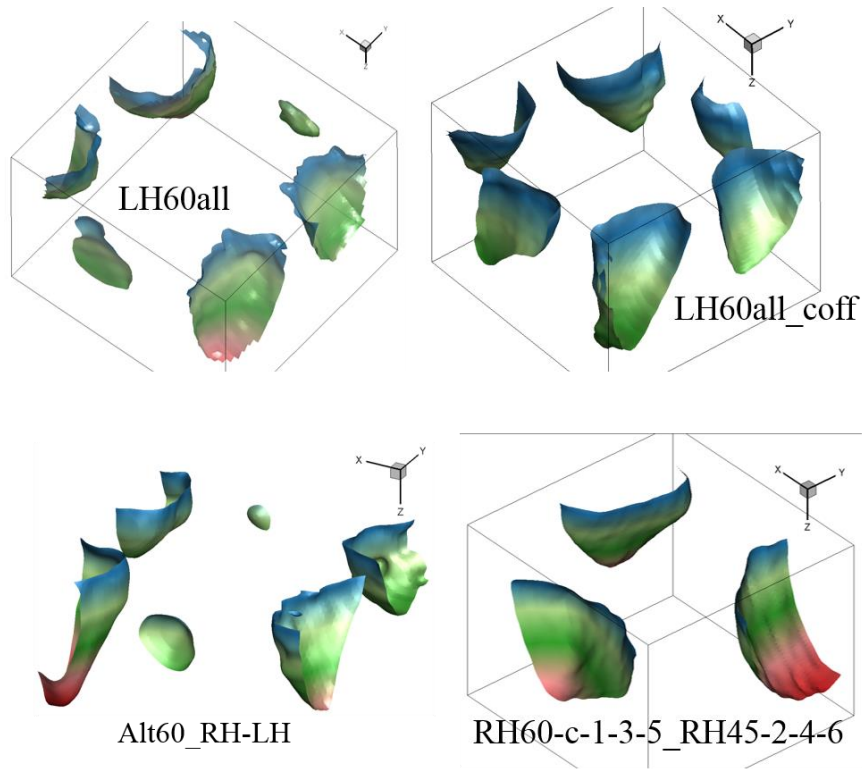


Figure 5 $V_z = 0$ envelopes outlining recirculation zones for those cases that do not exhibit a CRZ for the center swirler. Contours are colored by distance from the dump plane, blue is closest, red farthest. 800K, 5-bar. $U_{ref} = 22.9\text{-m/s}$

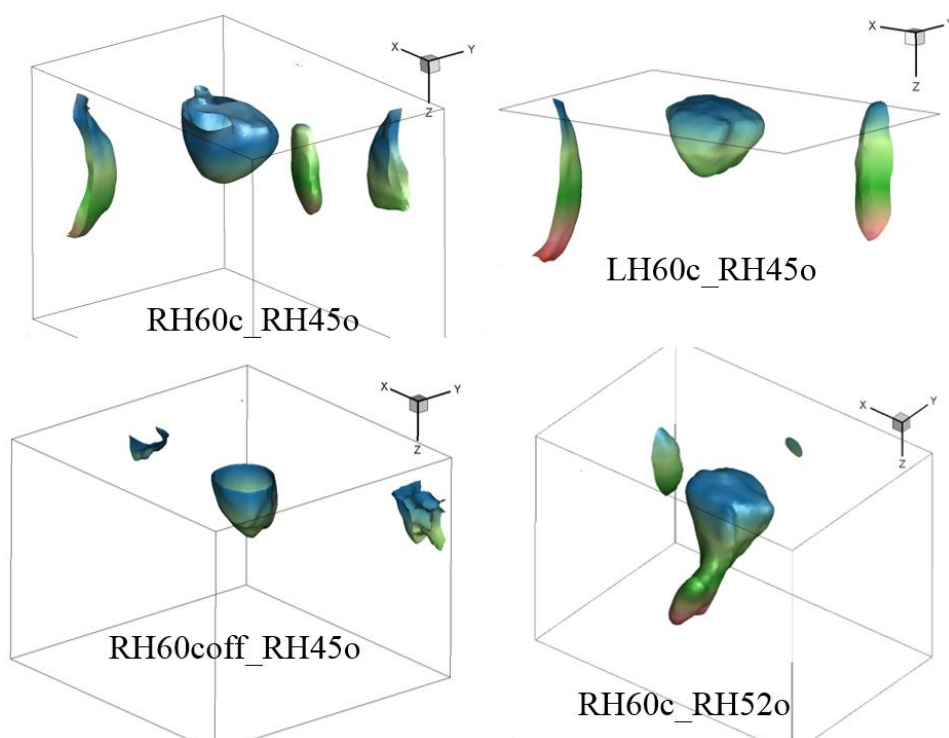


Figure 6 $V_z = 0$ envelopes outlining recirculation zones for those cases that exhibit a CRZ for the center swirler. There also exist in some places edge recirculation zones, ERZ near outer swirlers. Contours are colored by distance from the dump plane, blue is closest, red farthest. 800K, 5-bar. $U_{ref} = 22.9\text{-m/s}$

3.2.1 On center swirler CRZ formation

For this LDI-1 type 7-point array, we have seen interaction between the swirlers due to the closer spacing (compared to the 9-pt) that affects the flow. For instance, when all 60° swirlers are installed (figure 4, top row; figure 5), the close spacing is such that two of the opposing outer swirler CRZs are displaced away from the combustor centerline. The displacement is due to interaction of flow from the center swirler, because when the center swirler is recessed (thereby providing more isolation), all outer CRZs are positioned more directly downstream of their respective swirlers. (We are not certain at this time why only two of the six outer CRZs are displaced. It may have something to do with the way the fuel tubes and instrumentation are routed in the hardware just upstream, or where the swirler spokes are oriented with respect to the neighbouring swirlers.)

Another example of the recess effect is for the configurations having a RH 60° center swirler surrounded by RH 45° outer swirlers. With the recess, a high velocity region surrounds the CRZ, but without the recess, there is more separation or distinction of the fields between the outer swirlers.

In no case involving all 60° swirlers (top row) did we find a CRZ downstream from the center swirler. Interaction between the outer swirlers with the center swirler counteracts the center swirl, which prevents a CRZ from forming. There is still enough swirl from the outer swirlers so that each of the outer swirlers produces a CRZ. We saw little difference between the cases with all swirlers having the same orientation (left-handed) and with alternating LH-RH outer swirlers (compare figure 5 top row, right with left).

The only configurations that produce a CRZ downstream of the center swirler have a 60° in the center, surrounded by 45° or 52° swirlers; this result is as expected, given the 1-point LDI results that showed the narrow high-velocity field produced using those swirlers, which helps isolate the field produced by the center 60° swirler. However, for these 7-point configurations, there were recirculation zones—two or three—on the outer edges of some outer swirlers. These we term edge recirculation zones (ERZ), which are most obvious for the non-recessed 45° swirlers; and less obvious for the center offset and 52° swirler cases. The ERZs are probably similar to what are termed corner recirculation regions observed in computational studies of the 9-pt LDI [18].

The configuration that alternated RH60° with RH45° swirlers outside produced three very large CRZs behind the outer 60° swirlers. Based on the available data, we estimate the total volume of those three CRZs to be at least as large as the total volume for the configurations that have all 60° swirlers on the outside. This is consistent with the study conducted by Kao [19], which found that less-confined swirl produces larger recirculation zones.

The only configuration that produced no CRZ anywhere is the case with RH 52° swirlers at all positions. We chose to run this case despite not seeing a CRZ in the 1-LDI tests because CRZ formation seemed to be on the cusp of being possible. There were small pockets with reverse flow, but without sizable structure.

3.2.2 On counter-swirl

The gross effect of counter swirl is to isolate the flow from individual swirlers. For example, compare the fields from the all 60° swirler cases, the top row of figure 4, which shows from left to right the counter-swirl, center offset, and co-swirl cases. If we consider the offset case to be most isolated, it presents a six-sided star shape that bounds the high-velocity downstream core (bounded by the outer six swirlers). In the case having all co-flowing swirlers, the star shape is somewhat washed out and the vertices are not as well-defined. In the configuration having the alternating LH-RH outer swirlers, the star-shape pattern is more defined. The other counter-swirl comparison is with the RH 45° swirlers on the outside, with either a counter swirl (bottom left) or co-swirl (bottom center) 60° center swirler. In this comparison, the higher velocity flow behind the outer swirlers provides a somewhat narrower and nearly contiguous boundary around the center swirler, compared to the co-swirling case.

3.3 Comparing the four configurations that have a center swirler CRZ

In this section, we compare the four configurations that have a CRZ downstream of the center 60° swirler. There are three direct comparisons that differ by only one change. Those consider the “pilot” recess effect, the swirler clocking effect (co-swirl vs counter-swirl), and the outer swirler angle (45° vs 52°).

3.3.1 Comparison 1: RH60c_RH45o with and without center swirler recess (figures 6 - 8)

In the case of the center pilot recess, there exists a distinct CRZ that might be physically largest upstream of the dome exit, above the field of view. The axial velocity contour end view slices in figure 7 show an annular core of high downstream velocity surrounding the swirler at the dome exit that diffuses outward as it moves downstream, and forms a more-or-less triangular-shaped high velocity region. Without the center swirler recess (Figure 8), that high velocity annular region does not exist and one can see the high core flow from the individual outer swirlers. In both cases, there are smaller recirculation regions that form either at the outer edges and/or between some outer 45° swirlers. In the case with the offset, these ERZs appear relatively small (best seen in figure 6, left column).

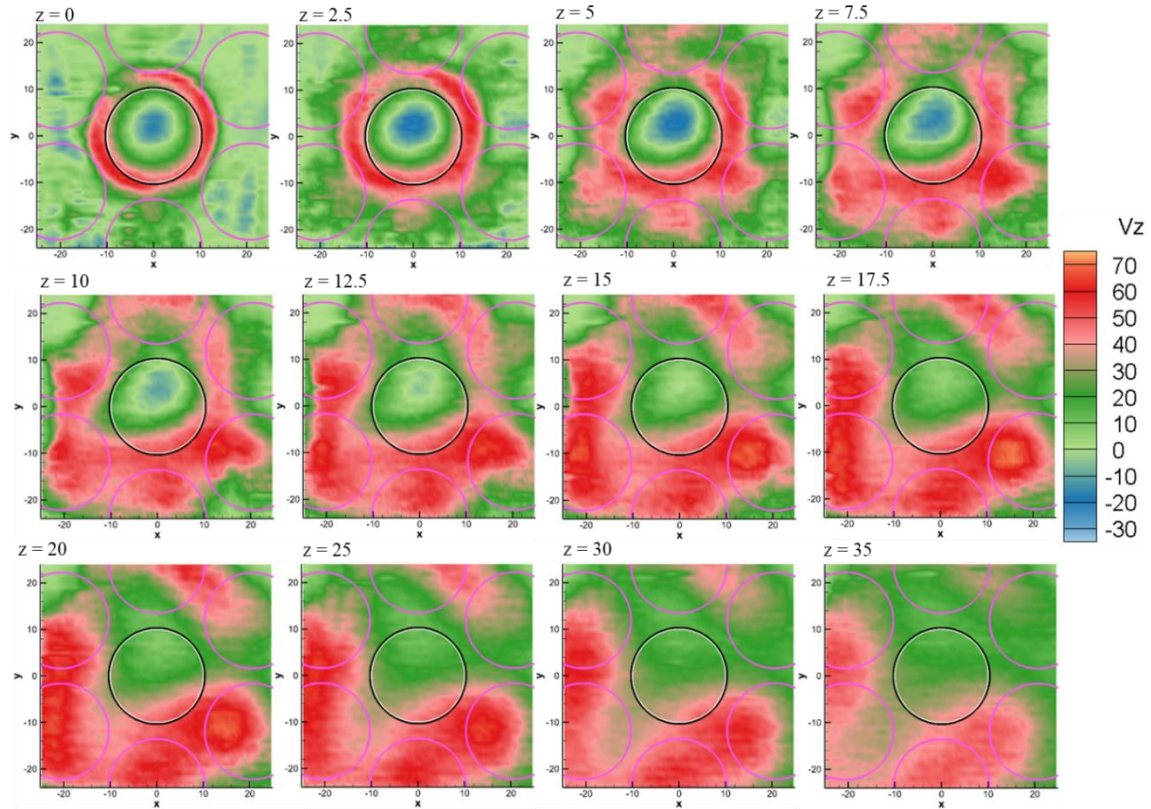


Figure 7 End views showing axial velocity contours at various distances from the dome exit. Configuration RH60coff_RH45o. See legend in figure 4. The axial location is noted for each slice. 800K, 5-bar. $U_{ref} = 22.9\text{-m/s}$

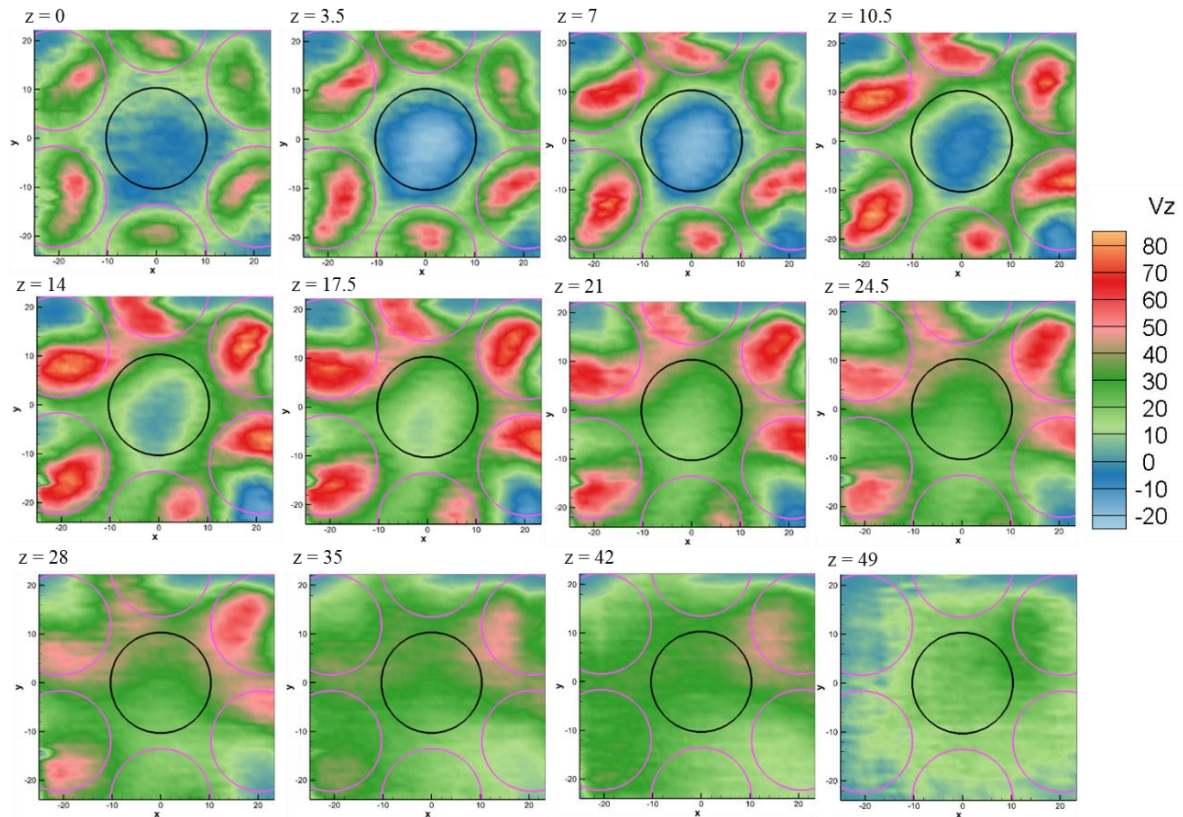


Figure 8 End view composites showing axial velocity contours at various distances from the dome exit. Configuration RH60c_RH45o. See legend in figure 4. The axial location is noted for each slice. 800K, 5-bar. $U_{ref} = 22.9\text{-m/s}$

3.3.2 Comparison 2: Swirler clocking effect

Swirler clocking effect, i.e. co-swirl vs. counter-swirl: RH45 outer swirlers with either LH60 or RH60 center swirler (figures 6, 8, 9)

Near the dump plane, the counter-swirl case, LH60c_RH45o, shows a relatively narrow band of high velocity air from each outer swirler on the side nearest the center swirler, where the CRZ forms. The narrow, high velocity bands show little curvature (compared to the co-swirling case) and forms a non-contiguous hexagonal boundary about the center swirler. In the co-swirling case, RH60c_RH45o, the corresponding high velocity bands are thicker and show more curvature, tending to follow more the shape of the swirler boundary. For both configurations, ERZs are formed within the field of view, (best seen in the overview iso-velocity surfaces, above). For both configurations, the ERZs extend farther downstream than do the CRZs. In the far field, roughly 50-mm downstream, the velocity field is more uniform for the co-swirl case, than for the counter-swirl configuration, probably because the reverse-flow ERZs extend farther downstream.

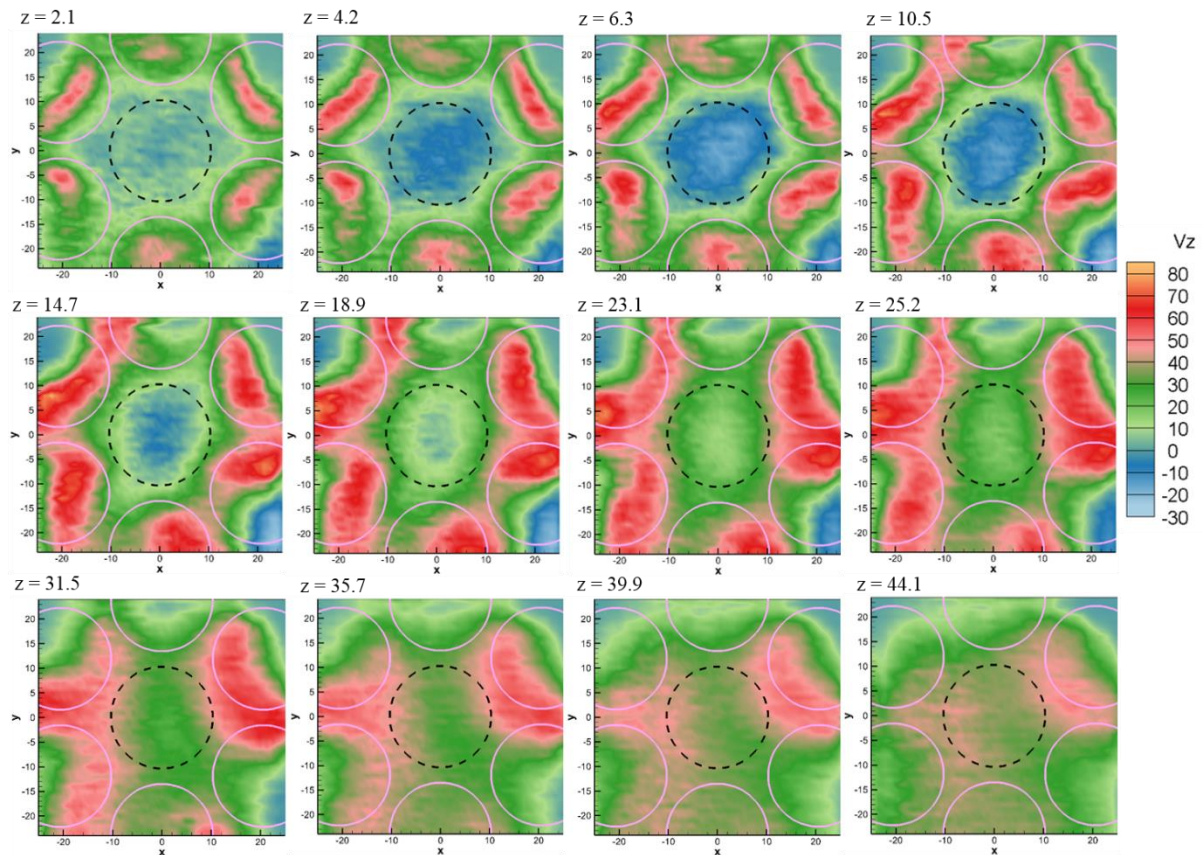


Figure 9 End view composites showing axial velocity contours at various distances from the dome exit. Configuration LH60c_RH45o. See legend in figure 4. The axial location is noted for each slice. 800K, 5-bar. $U_{ref} = 22.9\text{-m/s}$

3.3.3 Comparing 52° and 45° swirlers on outside, RH60cRH52o vs RH60cRH45o (figures 3, 6, 8, 10, 11)

One large difference between RH60c_RH45o and RH60c_RH52o is the extent of the central recirculation zone that develops downstream of the central 60° swirler. Near the dome exit, the CRZs are similar in shape, but for the case with the 52° swirlers, the CRZ has a tail that extends considerably farther downstream. The tail is also displaced away from the centerline as is most clearly demonstrated in the iso-velocity contour plots, but can also be seen in the figure 10 end views, which show the reverse flow region shifting in (-)y as s increases. The x-z plots for RH60c_RH52o in figure 11 show the velocity fields at $y = -12$, $y = 0$, and $y = 12$, and also emphasize the flow field asymmetry that develops with the 52° swirlers. Comparing the $y = 0$ position for this case with configuration RH60c_RH45o (figure 3, upper left), the CRZ is less isolated when the 52° swirlers are on the outside.

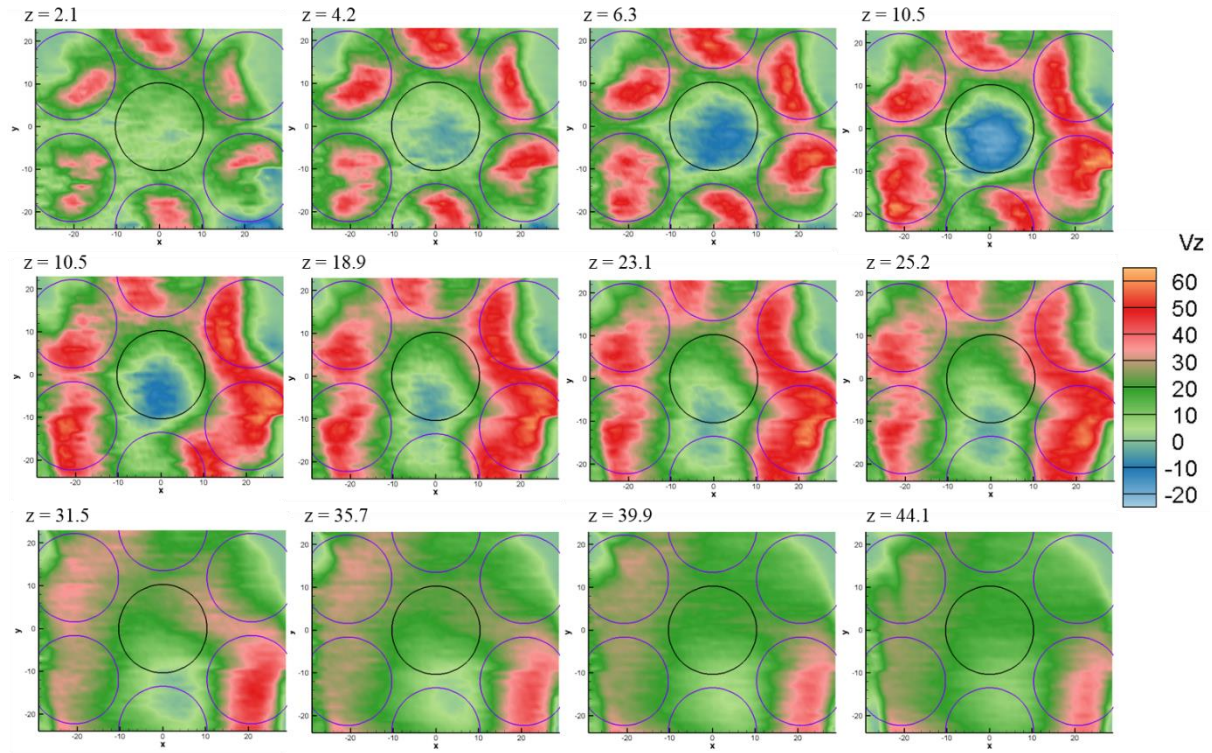


Figure 10 End views showing axial velocity contours at various distances from the dome exit. Configuration RH60c_RH52o. See legend in figure 4. The axial location is noted for each slice. 800K, 5-bar. $U_{ref} = 22.9\text{-m/s}$

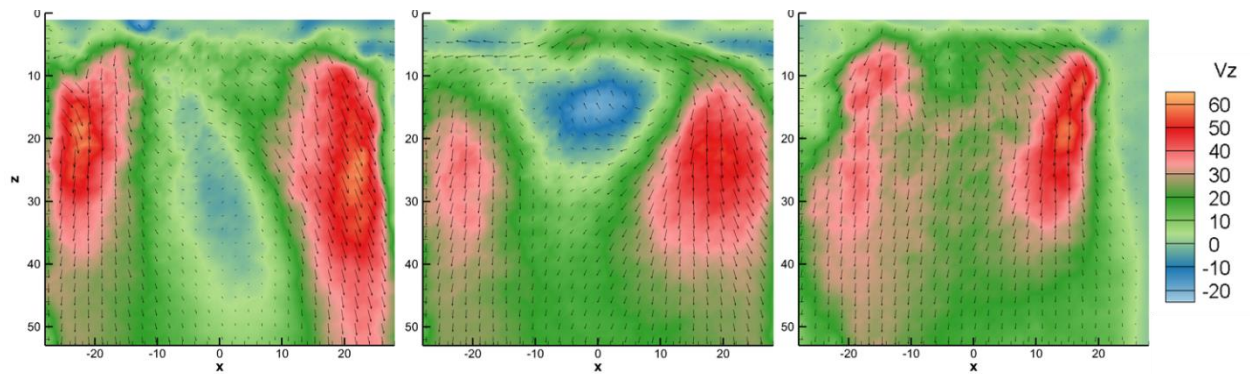


Figure 11 Results from RH60c_RH52o. Average 2D velocity vectors and contour of axial velocity at positions $Y = -12$ (left), $Y = 0$ and $Y = +12$ are shown. Flow is from top to bottom. 800K, 5-bar. $U_{ref} = 22.9\text{-m/s}$

3.3.4 Recirculation zone size and strength

We estimated the volume of the center recirculation zones for those configurations with a center swirler CRZ, using the integration feature in Tecplot. The results are shown in figure 12. We used the non-smoothed values of axial velocity to define the CRZ volume. (The effect of using the smoothed versions for volume resulted in slightly smaller volumes, but the trends were the same.) We saw little difference between the volumes for the configurations with 45° and 52° , but show a larger difference in the overall shape of the CRZ as shown in figure 6. In the case with the 45° swirlers, the recirculation zone does not extend very far downstream, but does for the 52° swirler. We also show the average axial velocity within the CRZ, which trends with the CRZ volume. This trend is in agreement with Kao [ref], who found that the larger the CRZ, the higher the magnitude of reverse velocity.

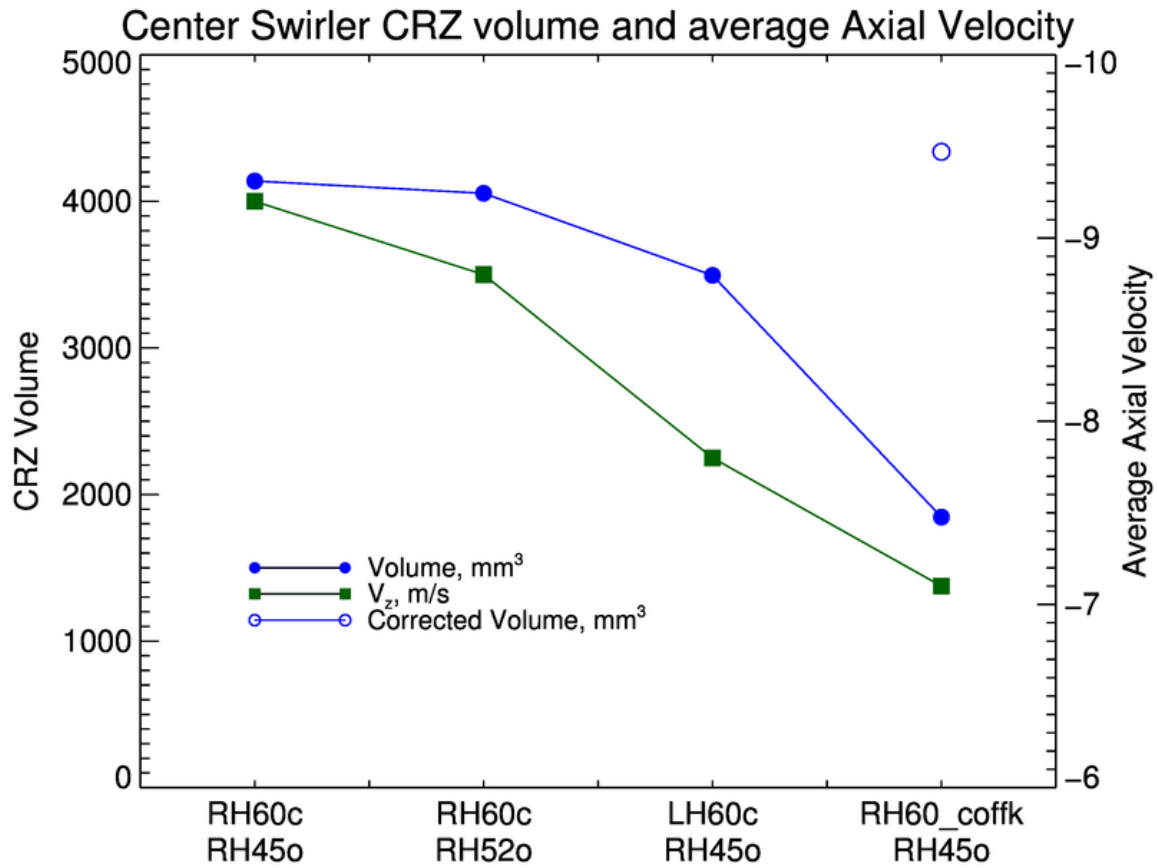


Figure 12 Chart showing the estimated CRZ volume (left y-axis) and axial velocity (right y-axis) for the configurations shown on the x-axis

3.4 Combusting Results

To date, we have run combustng tests using all co-swirling 60° configurations, either LH60all or RH60all. This is the baseline configuration, and is used also for investigating dynamics and for studying the mitigation of high dynamic conditions, either passively or actively. Thus, we have had limited testing for operability (range of stable conditions) and emissions. We recently burned using the RH52all, RH60c_RH52o, RH60c_RH45o, and LH60c_RH45o. We have found that the all 60°swirler configurations are most operable, most likely because of the greater likelihood of CRZs present to act as flame holders. The configurations that had 45° swirlers were the least stable, and those with the 52°swirlers were a bit more stable in that we could operate at higher reference velocities. We also saw in the cold flow results that no CRZ formed using the RH52all configuration. Under combustng conditions, on average, RH52all burned relatively far downstream, roughly 22-mm. Run at similar inlet conditions, all other configurations had the flame stabilize at or within 5-mm of the dome. Figure 13 illustrates the difference between RH52all (top row) and RH60cRh52o. The left column shows the average chemiluminescence image intensity; the right column is RMS. Horizontal white lines mark the dome location, with flow from top to bottom. It is interesting to note that the luminous structure in RH60c_RH52o has a shape similar to the cold flow CRZ shown in figure 6.

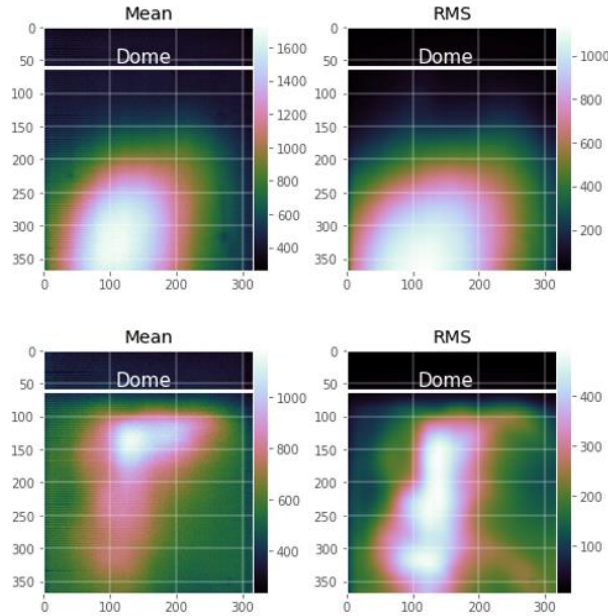


Figure 13 Comparing flame standoff for configurations RH52all (top) and RH60c_RH52o for mean signal intensity(left) and the RMS (right). Units are pixels

3.4.1 Dynamics results—sample results from combustion testing

Figure 14 shows the power spectra of P_4 (left) and flame luminosity (right). From top to bottom, the rows are RH52all, RH60c_RH52o, RH52all, RH60c_RH45o, and LH60all. For the top two rows, the inlet conditions are matched. All others are different, and shown in the annotations provided for each row.

A few things to point out with regard to the power spectra are:

1. while both P_4 and flame luminosity power spectra have frequencies in common, the dominant frequency may be different for each (as illustrated in the third row, RH52all)
2. what frequencies appear depends on the inlet conditions, compare both RH52all cases
3. some frequencies may show up in one, but not in the other, such as in RH60c_RH45o

With these observations in mind (especially point 2), we note that there were three consistent dominant frequencies: near 400-500 Hz, near 700-800 Hz, and near 1100-1200 Hz. For all configurations except the RH52all, the most common dominant frequency was near 700-800 Hz such as seen in the bottom two rows of figure 14. In particular, at light-off conditions, the near-700-800 Hz frequency was dominant for every configuration except RH52all. In fact, for the RH52all configuration, there were no conditions for which the near 700-800 Hz peak was dominant. There were dominant frequencies near 400-500 Hz and near 1100-1200 Hz for nearly every configuration. (The only exception was the LH60c_RH45o, for which there was limited data.)

Because there was a single dominant 500-Hz peak for the both the RH52all and RH60cRH52o configurations at the same inlet conditions, we thought it would be interesting to explore what was happening at 500-Hz. It was also convenient that the division of 40,000 by 500 is an integer, and so simpler to work with when ensemble averaging images to determine the 500-Hz phenomena.

3.4.2 Phenomena near 500-Hz

The remaining discussion describes what we saw when we isolated the region near 500-Hz for configurations RH52all and RH60c_RH52o.

Figure 15 shows the ensemble RMS and the normalized spectra near 500-Hz. They were derived using the original set of 48000 or so images, obtained at 40,000-Hz. A small sample of typical original images is shown in the top row of figure 16. Since we are interested in periodic phenomena occurring at a frequency near 500-Hz, we can sample the original dataset with a period of 2 msec (every 80 images) and compute ensemble average for the sample. We then step along the image sequence and repeat the process. Typical results of this process are shown

in the middle row of figure 16. For each of these ensemble averaged images, we subtract the mean of the original set to reveal the chemiluminescent structure at 500-Hz.

Figures 17 and 18 are the results for the 80 time steps obtained using the procedure just described. The RH52all configuration shows small scale structure, whereas the RH60c_RH52o configuration seems to show a larger, coherent structure (there is a CRZ in this case), which we think is due to its precessing vortex core.

To get a sense of how fast the flame front moves axially (as defined by where the most intense light is), we produced a mapping of intensity as a function of time, using the image sequences in figures 17 and 18. Each image in figure 19 collapses a single image into a column by summing the pixels in each row. For example, we take the image in the upper left corner of figure 17 which is an ensemble average starting at time 0 msec and add up pixels in each row. This vector of sums becomes the first column in Figure 19. The resulting graphs help visualize how the peak intensity moves in the axial direction. For the RH60c_RH52o configuration, the peak signal moves downstream in the images at a rate of approximately 217 pixels/ms, which translates to roughly 33-m/s, and up toward the dome at about half that rate.

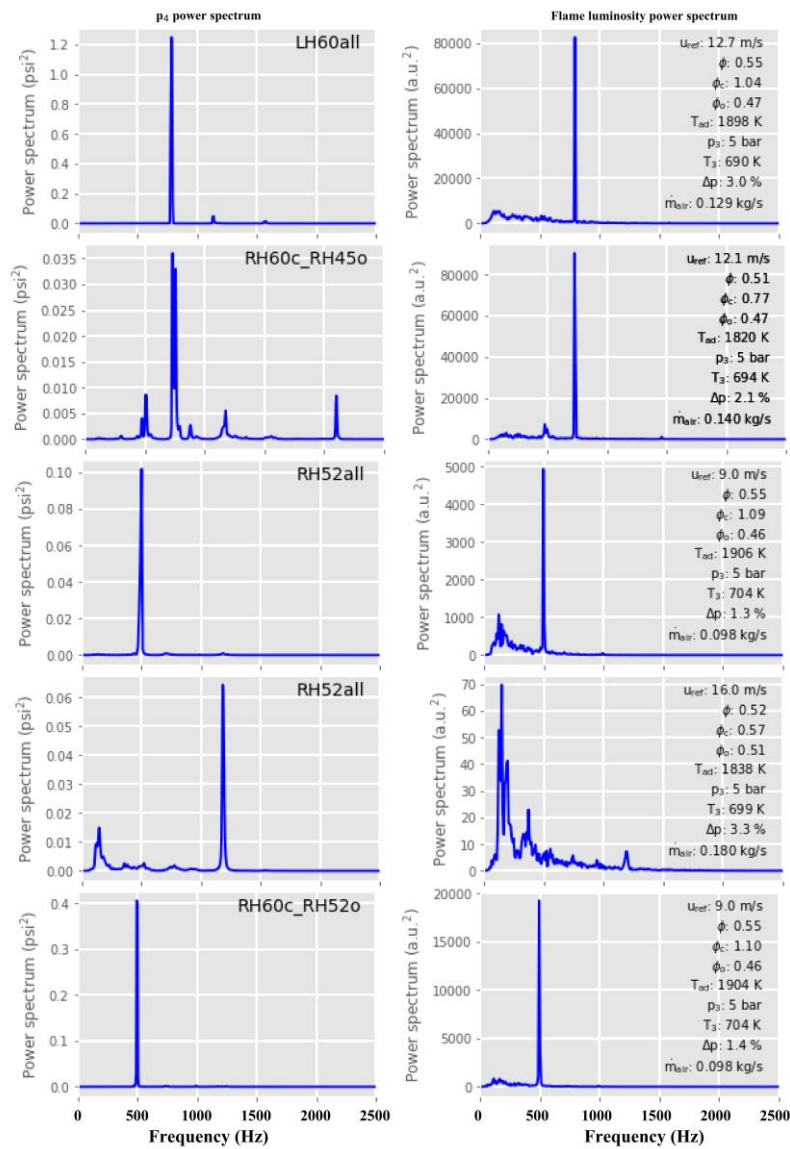


Figure 14 P4 power spectra (left column) and Chemiluminescence power spectra (right column) for the configurations and conditions indicated on each row

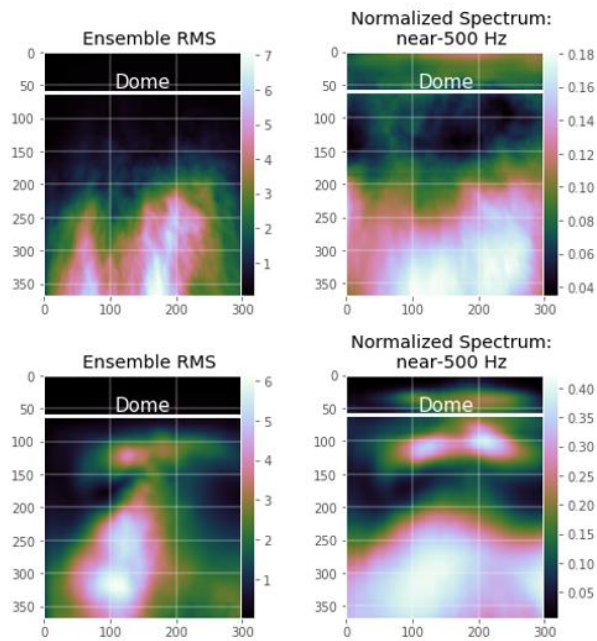


Figure 15 Images of the ensemble RMS (left) and the normalized spectrum (right) images near 500-Hz for configurations RH52all (top) and RH60c_RH52o

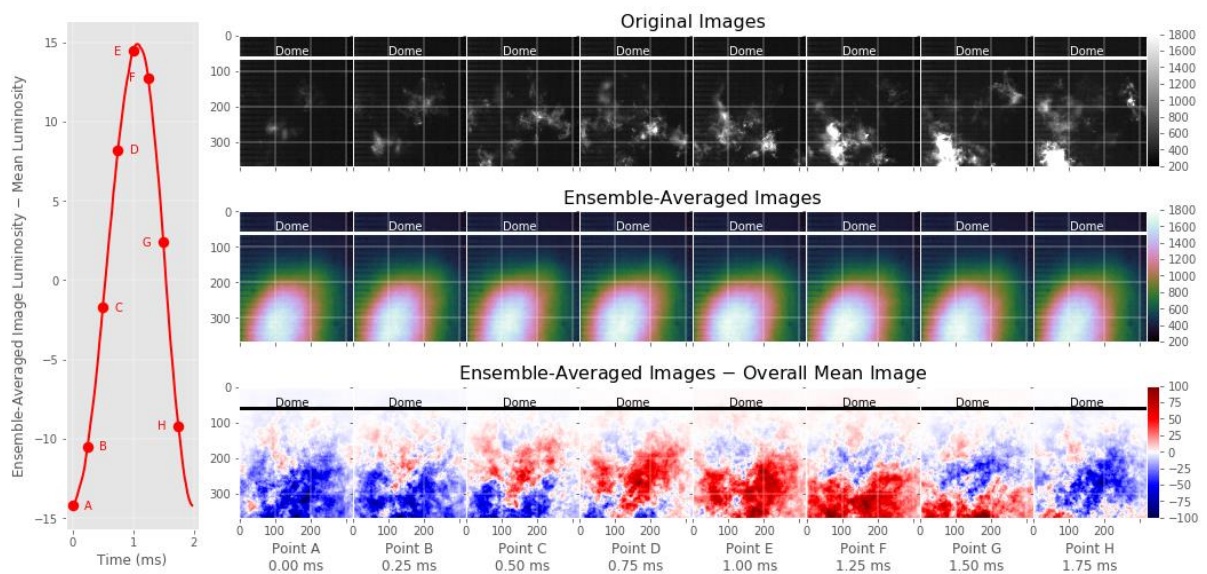


Figure 16 Example to describe the procedure used to isolate and reveal the 500-Hz phenomena within the flame chemiluminescence images. Top row shows a series of original images. Middle row shows ensemble-averaged images, resampling the image set at 500-Hz. Bottom

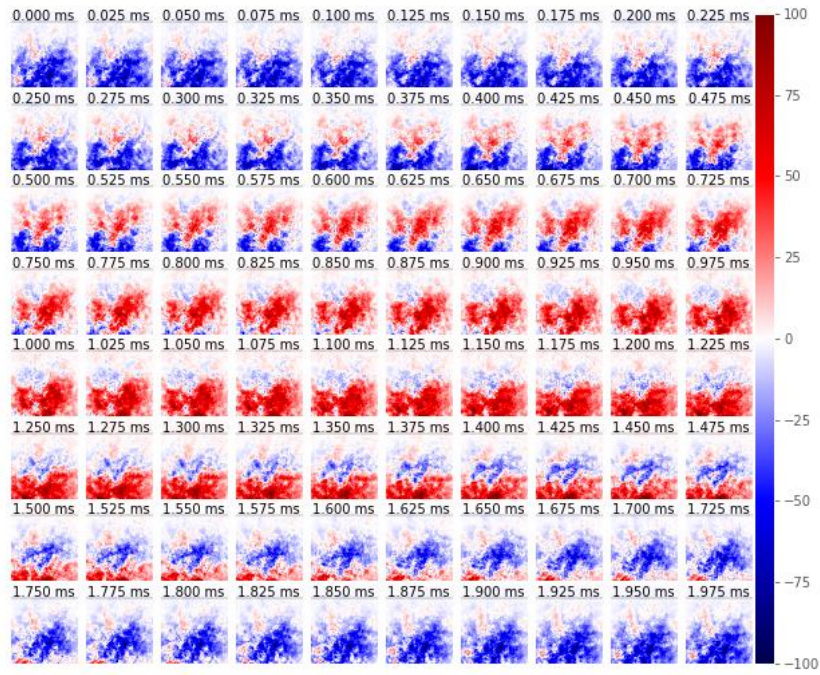


Figure 17 Series of (ensemble average – overall mean) images, that reveal the underlying structure at 500-Hz. The time step between images is 0.025-ms. Configuration RH52all

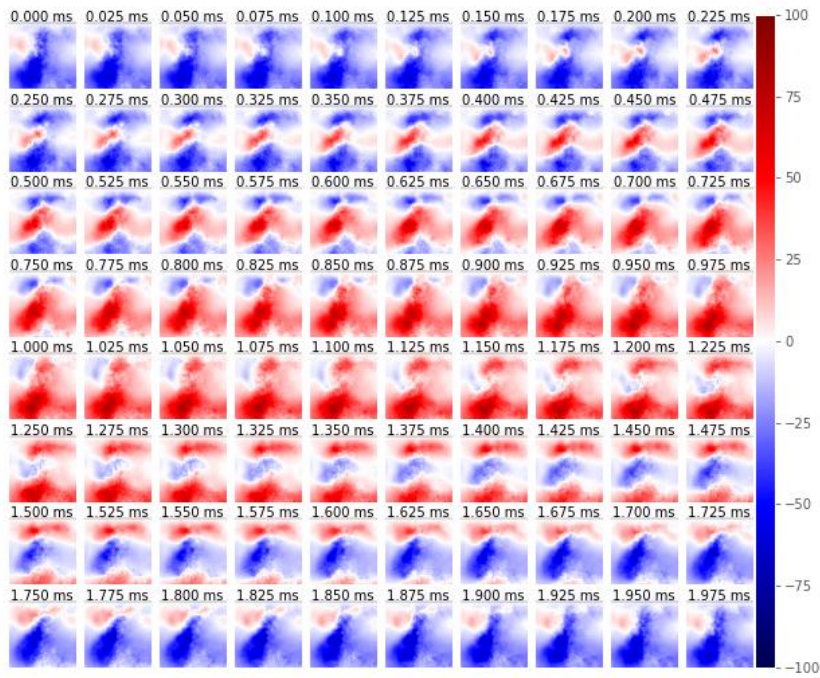


Figure 18 Series of (ensemble average – overall mean) images, that reveal the underlying structure at 500-Hz. The time step between images is 0.025-ms. Configuration RH60c_RH52o

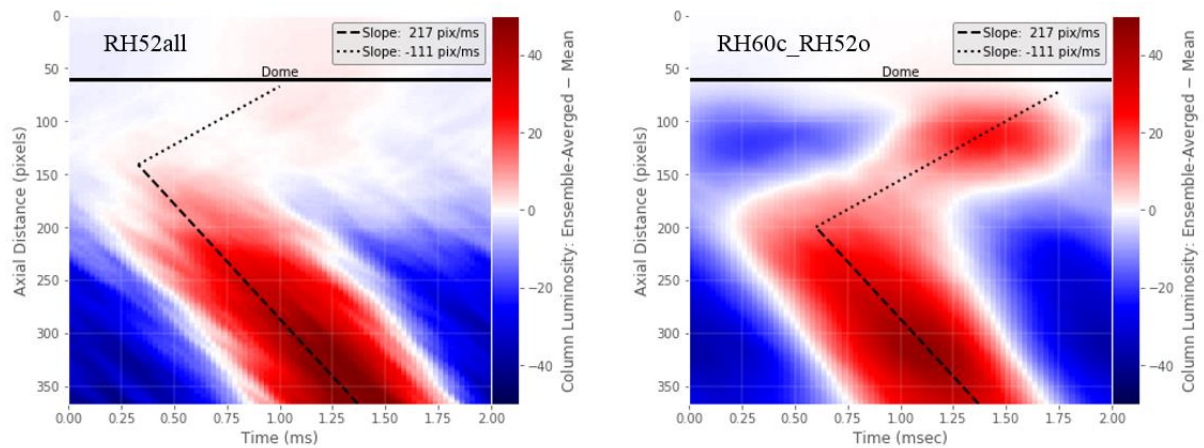


Figure 19 Trajectory of flame chemiluminescence over time for 7-LDI swirler configurations RH52all and RH60c_RH52o

4.0 SUMMARY

We have presented results of a cold flow parametric survey to explore center recirculation zone formation, size, and strength for nine swirler configurations of a 7-pt LDI array. From the cold flow examination, we found that

- Of the three swirlers, only the 60° swirler ($SN = 1$) produced a CRZ
- The close spacing of swirler elements in the array definitely leads to interactions between swirlers
- Recessing the center element helps to isolate it from the surrounding swirlers
- Using counter swirl helps to isolate the swirlers
- Inter-element spacing affects the size and strength of the CRZs

We also presented results obtained by spectral analysis of five configurations, with a focus on exploring 500-Hz events. In addition to the pressure signals, we are able to make use of the high speed images to identify dynamics from the flames. Despite our limited combustion testing, we also have identified another method to reveal flow structure at frequencies of interest and can possibly use this method to determine flame speeds. We expect to explore this method further to help possibly identify sources of dynamics.

ACKNOWLEDGMENTS

This work was supported by the Transformational Tools and Technologies Project under the NASA Aeronautics Research Mission Directorate.

REFERENCES

- [1] R TACINA, C-P MAO, C WEY, "Experimental investigation of a multiplex fuel injector module with discrete jet swirlers for low emission combustors," Paper AIAA , 2004-135, 2004
- [2] R TACINA, C WEY, K CHOI, "Flame tube NO_x emissions using a lean-direct-wall-injection combustor concept" NASA/TM—2001-211105 and Paper AIAA-2001-3271, 2001.
- [3] R TACINA, C WEY, P LAING, A MANSOUR, "A low NO_x lean-direct injection, multipoint integrated module combustor concept for advanced aircraft gas turbines," NASA/TM—2002-211347, 2002.
- [4] R TACINA, P LEE, C WEY, "A lean-direct-injection combustor using a 9 point swirl-venturi fuel injector," ISABE-2005-1106, 2005
- [5] K AJMANI, P LEE, H MONGIA, "CFD computations of emissions for LDI-2 combustors with simplex and airblast injectors," Paper AIAA2014-3529, 2014
- [6] K M TACINA, C T CHANG, Z J HE, P LEE, B DAM, H MONGIA, "A Second Generation Swirl-Venturi Lean Direct Injection Concept," AIAA-2014-3434, 2014

- [7] K M TACINA, D P PODBOY, Z J HE, P LEE, B DAM, H MONGIA, "A comparison of three second-generation swirl-venturi lean direct injection combustor concepts," Paper AIAA 2016-4891, 2016
- [8] K AJMANI, H C MONGIA, P Lee, "Parametric design of injectors for LDI-3 combustors," Paper AIAA 2015-3785, 2015
- [9] C HUANG, C YOON, R GEJJI, W E ANDERSON, V SANKARAN, "Computational study of combustion dynamics in a single-element lean direct injection gas turbine combustor," Paper AIAA 2014-3433, 2014
- [10] J C DELAAT, D E PAXSON, "Characterization and simulation of the thermoacoustic behaviour of an advanced, low emissions combustor prototype,," NASA TM—2008-215291, AIAA 2008-4878, 2008
- [11] D G LILLY, "Swirling flow in combustion: a review," *AIAA Journal*, Vol. 15, No 8, pp.1063-1078, 1977.
- [12] W A ACOSTA, C T CHANG, "Experimental combustion dynamics behaviour of a multi-element lean direct injection (LDI) gas turbine combustion", AIAA 2016-4589, 2016.
- [13] S A TEDDER, K M TACINA, R C ANDERSON, Y R HICKS, "Fundamental study of a single point lean direct injector. Part I: Effect of Swirler Angle and Injector Tip Location". Paper AIAA 2014-3435, 2014.
- [14] C M HEATH, R J LOCKE, R C ANDERSON, Y R HICKS, "Optical Characterization of a Multipoint Lean Direct Injector for Gas Turbine Combustors: Velocity and Fuel Drop Size Measurements", IGTI, GT2010-22960, 2010
- [15] Y R HICKS, C M HEATH, R C ANDERSON, K M TACINA. "Investigations of a Combustor Using a 9-Point Swirl-Venturi Fuel Injector: Recent Experimental Results," Paper ISABE-2011-1106, NASA/TM-2012-217245, 2012
- [16] Y R HICKS, K M TACINA, R C ANDERSON, S A TEDDER, "A comparison of flow fields generated by varying air swirler configurations in a 7-point lean direct injector array," presentation paper number 145IC-0035, Central States Section of the Combustion Institute, 2016
- [17] J M BEER, N A CHIGIER, "Combustion Aerodynamics", 1st ed., John Wiley & Sons, Inc., New York, 1972.
- [18] K AJMANI, H C MONGIA, P LEE, "Evaluation of CFD Best Practices for Combustor Design: Part I—Non-Reacting Flows," AIAA-2013-1144, 2013
- [19] Y H KAO, "Experimental Investigation of Aerodynamics and Combustion Properties of a Multiple-Swirler Array", Dissertation, University of Cincinnati, 2014